Mpox virus spreads from cell-to-cell and leads to neuronal injury in human cerebral organoids

Isabel Schultz-Pernice[1,2,3,§], Amal Fahmi[1,2,3,§], Yen-Chi Chiu[4,5], Blandina I. Oliveira Esteves[1,2], Teodora David[1,2], Antoinette Golomingi[1,2], Beatrice Zumkehr[6], Damian Jandrasits[3,7], Roland Züst[7], Selina Steiner[6], Carlos Wotzkow[6], Fabian Blank[6,8], Olivier B. Engler[7], David Baud[4,5], and Marco P. Alves[1,2,9,*]

[1]Institute of Virology and Immunology, Bern, Switzerland

[2]Department of Infectious Diseases and Pathobiology, Vetsuisse Faculty, University of Bern, Bern, Switzerland

[3]Graduate School for Cellular and Biomedical Sciences, University of Bern, Bern, Switzerland

[4]Materno-Fetal and Obstetrics Research Unit, Department "Femme-Mère-Enfant", Lausanne University Hospital, Lausanne, Switzerland

[5]Faculty of Biology and Medicine, University of Lausanne, Lausanne, Switzerland

[6]Department for BioMedical Research, University of Bern, Bern, Switzerland

[7]Spiez Laboratory, Austrasse, 3700 Spiez, Switzerland

[8]Department of Pulmonary Medicine, Inselspital, Bern University Hospital, Bern, Switzerland

[9]Multidisciplinary Center for Infectious Diseases, University of Bern, Bern, Switzerland

[§]These authors contributed equally

*Correspondence: marco.alves@unibe.ch (M.P.A.)

ABSTRACT

In 2022-23 the world experienced the largest recorded mpox virus (MPXV) outbreak outside of endemic regions. Remarkably, cases of neurological manifestations were reported, some of which fatal. MPXV DNA and MPXV-specific IgM antibodies were detected in the cerebrospinal fluid of encephalitis-affected patients, suggesting neuroinvasive potential of MPXV. We explored the susceptibility of neural tissue to MPXV infection using human cerebral organoids (hCOs) exposed to a primary isolate belonging to clade IIb lineage. The virus efficiently replicates in hCOs as indicated by the exponential increase of infectious viral loads and the elevated frequency of MPXV-positive cells over time. Also, electron microscopy imaging revealed the presence of viral particles as well as perinuclear viral factories. We observed susceptibility of several cell lineages to the virus, including neural progenitor cells, neurons, and astrocytes. Furthermore, we detected the presence of viral antigens in neurites and in foci of grouped cells distributed throughout the tissue. In line with this, examining released and cell-associated MPXV titers, we observed significantly more cell-associated infectious virus, suggesting viral spread by cell-to-cell contact. While hCOs displayed no evident outer morphological changes upon infection, we detected the formation of varicosities in neurites, pointing to viral manipulation of axonal transport and neuronal injury. In accordance, the apoptosis marker cleaved caspase-3 was detected within neurite swellings. Our findings identify a mechanism potentially contributing to MPXV-mediated neuropathology that may have therapeutic implications.

Keywords: mpox, monkeypox, orthopoxvirus, zoonosis, neural organoids, cerebral organoids, brain organoids, encephalitis, axonal beading, neuron injury.

INTRODUCTION

The first case of mpox virus (MPXV) infection without traceable contact to African population or fauna was registered in UK in early May 2022[1]. Since then, more than 100 countries reported cases of infection[1], marking the largest recorded MPXV epidemic outside of African countries. First manifestations of MPXV infection observed during the current outbreak include fever, lethargy, myalgia, lymphadenopathy and headache, followed by skin lesion[2-4]. While most clinical cases recorded during the epidemic were observed to be mild[2,4], severe complications may develop. From 1985 to 2021, serious neurological manifestations, including confusion, seizures and encephalitis, have been recorded in around 3% of MPXV infected patients[5], including one fatal case[6]. Since May 2022, encephalitis has been diagnosed in several patients affected by MPXV infection[7-14], including two young, healthy men that died following the complications[7]. Animal studies have suggested neuroinvasive potential of MPXV, detecting viral DNA in the brain of several rodent species[15-18]. This hypothesis is further supported by the detection of MPXV DNA in the cerebrospinal fluid (CSF) of one affected woman during this outbreak[10] as well as the detection of MPXV-specific IgM antibodies in the CSF of a 6-year-old girl in 2003[19].

Despite first reports of deadly encephalitis cases dating back to 1987[6], mechanisms driving acute neurological manifestations during MPXV infections have been poorly investigated in the human host. Possible causes include the previously restricted geographical distribution of the virus, as well as limited availability of material and accurate models to analyze the neuropathology in the human brain. In the past years, advanced three-dimensional (3D) cell culture systems have demonstrated their capability to recapitulate processes shaping human organs in health and disease. Moreover, these *in vitro* systems have provided unprecedented opportunities to study host-pathogen interactions in the human host exploiting a complex system accessible to experimental manipulation. In this study, we evaluated the susceptibility of neural tissue to MPXV infection using human cerebral organoids (hCOs), also known as brain or neural organoids, a sophisticated *in vitro* model closely mimicking human brain.

53 **RESULTS**

54 **Neural progenitor cells, astrocytes and neurons are susceptible to mpox virus infection**

55 The generation of hCOs from embryonic stem cells (ESCs) was performed according to
56 established methods (Supplementary Fig. 1a)[20]. To phenotype our cultures, hCO tissue of
57 different developmental stages was sampled over a period of 112 days and processed for
58 immunofluorescence characterization using well-established cell type markers to discriminate
59 between class III β-tubulin (TUJ1) expressing neurons[21-24] and sex-determining region Y-box
60 2 (SOX2) positive neural progenitor cells (NPCs)[25,26]. During the first days of development,
61 hCOs were observed encompassing high numbers of tightly clustered, small ventricular units,
62 previously described as fluid-filled cavities[20] surrounded by a compact but relatively thin sheath
63 of SOX2-expressing NPCs (Fig 1a, top panels). Isolated TUJ1-positive neurons were
64 occasionally observed scattered around the ventricles. Throughout the first and second month
65 of development, hCOs displayed increasing degrees of complexity, acquiring a typical layered
66 organization[20]. By day 60 of tissue expansion, enlarged ventricles surrounded by several
67 layers of tightly gathered NPCs became evident (Fig. 1a, central panels). Densely packed
68 TUJ1-expressing neurons surrounded the ventricular units, forming a thick meshwork of
69 perikarya and neurites (Fig.1a, central panels). Finally, a nuclei-poor outer layer was observed
70 on the organoid's basal surface (Fig. 1a, central panels). As development progressed further,
71 organoids were observed losing ventricular organization, displaying a scattered population of
72 SOX2-positive cells nested within a neuron-dominated environment (Fig. 1a, bottom panels).
73 Furthermore, astrocytes, characterized by GFAP expression[27] in absence of SOX2 signal,
74 were observed appearing in hCOs by the third month of maturation, in line with previous
75 findings reporting the presence of astrocytes in minor numbers by day 45 of organoid
76 development[28].

77 Aiming to shed further light on the dynamics of MPXV replication within human neural tissue,
78 we set out to analyze its tropism within our cultures. Four independent batches of hCOs of 70-
79 95 days of age were exposed to a 2022 primary isolate of MPXV belonging to clade IIb lineage.
80 The infected hCOs were processed for immunofluorescence analysis. In line with recent

81 findings[29], we observed viral antigen localizing to the cytoplasm of SOX2-expressing cells (Fig.
82 1b, top panels), indicating susceptibility of NPCs to MPXV infection. Likewise, SOX2-negative
83 but GFAP-expressing astrocytes were confirmed to display viral antigen signal within cell
84 somata and extensions (Fig. 1b, central panel). In contrast to previous reports[29], hCO-derived
85 neurons were observed to be susceptible to MPXV infection as well, as viral antigen was
86 identified co-localizing with TUJ1 in both perikarya and neurites (Fig. 1c, bottom panels).
87
88 **Mpox virus replicates and spreads from cell-to-cell in human cerebral organoids**
89 We next set out to analyze the dynamics of MPXV replication by exposing hCOs to a low
90 multiplicity of infection (MOI) of 0.1 $TCID_{50}$/cell. Images, samples of tissue and supernatant
91 were collected till 10-14 days post-infection (p.i.; Supplementary Fig. 1b). No evident
92 alterations between mock-treated and MPXV-infected cultures were observed in outer
93 morphology at any time point tested. In addition, no significant or pronounced differences
94 emerged through surface area analysis of hCOs, with mock-infected organoids displaying an
95 average surface area over all time points of 13.0 mm^2, with an increase of 5.6 mm^2, compared
96 to MPXV-challenged hCOs, that showed a mean size of 13.4 mm^2 and 4.8 mm^2 growth.
97 Viral replication and distribution in the tissue over time was investigated through
98 immunofluorescence analysis. Viral particles were highlighted using an antibody targeting the
99 viruses' A27L protein, a conserved and multifunctional viral envelope protein known to mediate
100 viral attachment and fusion to cell surfaces, as well as transport of the related vaccinia virus
101 through microtubule interaction[30-32]. While no viral antigen was visible in mock-treated hCOs,
102 small gatherings of MPXV-positive cells were detected in infected cultures as early as day 2
103 p.i. (Fig. 2a). Viral antigen signal was subsequently observed steadily increasing over time,
104 reaching a peak at day 10 p.i., at which numerous elliptical and elongated infection foci became
105 evident around the organoid's perimeter (Fig. 2a), alongside streams of infected cells and
106 scattered single cells reaching deep into the hCO core. Between day 10 and day 14 p.i., MPXV
107 signal reached its peak of intensity, as no further increase could be detected (Fig. 2a).

108 Strikingly, MPXV antigen was observed displaying a clustered distribution with positive cells
109 arranged in delimited foci at the hCO's surface layers (Fig. 2a).
110 Neural cell susceptibility to MPXV infection was further confirmed via transmission electron
111 microscopy of organoids collected 10 days p.i. Pleomorphic, intracellular mature virions,
112 characterized by a cuboid or ovoid structure with a central biconcave core were clearly visible
113 within cells of the analyzed tissue (Fig. 2b'), and represented the majority of observed viral
114 particles. Intracellular mature virions were visualized both in proximity to viral factories, and
115 approaching the cell's periphery, including regions of cell-to-cell contact. In addition,
116 perinuclear viral factories, containing viral particles at different stages of replication, were
117 observed on multiple occasions (Fig. 2b''). Viral crescent membranes at several stages of
118 maturation were observed, along with immature viral particles, characterized by a smooth
119 membrane encircling material of variable density (Fig. 2b''), previously suggested to indicate
120 different stages of virion organization[33]. Condensed cytoskeletal components were frequently
121 documented in proximity of viral factories (Fig. 2b''). Infected cells were commonly observed
122 in clusters, and displayed features described to appear at advanced stages of viral
123 replication[33], including immature viral particles not only in nuclear proximity but also
124 approaching host cell membrane, sustained nuclear morphology, and cytoskeletal
125 condensations. In addition, we identified cells displaying evident signs of cytopathic effect, with
126 nuclear degeneration and membrane rupture, leading to virus release (Fig. 2c). Extracellular
127 virions without any evident association with cell structures were occasionally observed within
128 hCO tissue. Further stages of viral particle maturation, including intracellular enveloped virions
129 and cell-associated enveloped virions, were not identified.
130 The vaccinia virus has been described exploiting several mechanisms to spread from cell-to-
131 cell, including the formation of actin tails[34,35] and tunneling nanotubules (TNTs)[36]. Through
132 transmission electron microscopy, we captured viral particles localizing not only to cell somata,
133 but also to tube-like cellular extensions, rich in cytoskeletal components, reminiscent of
134 neurites (Fig. 2d). In line with this observation, detailed immunofluorescence analysis revealed
135 infection not only limited to cell somata, but extending into thin cell filaments, frequently

136 spanning between two cells within infection foci (Fig. 2e) and disseminated within the
137 organoid's cell meshwork. To elucidate the nature of documented tubular structures, we
138 performed co-localization analysis of viral antigen signal with F-actin and neuronal marker
139 TUJ1, allowing discrimination between TNTs and neurites[37]. Infected filaments of different
140 length staining positive for both F-actin and TUJ1 were detected spanning between cells,
141 confirming MPXV localization within neurites (Supplementary Fig. 2a, yellow arrowheads). In
142 addition, viral antigen accumulation within F-actin positive, but TUJ1 negative cell-connecting
143 filaments, was occasionally observed (Supplementary Fig. 2a, blue arrowheads), suggesting
144 MPXV dissemination into, and possibly through, peripheral cell projections of variable nature.
145 Intrigued by the observed viral distribution within filamentous structures, we set out to
146 investigate the presence of cell-to-cell transmission among hCO cells. To discriminate between
147 released and cell-associated infectious virus, we performed titrations of both supernatant and
148 homogenized hCOs. At all measured time points, cell-associated viral titers were observed to
149 exceed released infectious virus, with differences spanning over several orders of magnitude
150 (Fig. 2f). Significantly higher cell-associated than released viral concentrations were detected
151 across all analyzed batches starting as early as day 2 p.i. and up to day 10 p.i., with most
152 pronounced divergence seen at day 10 p.i. (Fig. 2f). Cell-associated virus consistently
153 contributed to more than 90% of total infectious virus, with percentages fluctuating between 93
154 and 98% (Fig. 2g).
155
156 **Mpox virus infection leads to neurite injury in human cerebral organoids**
157 Further analysis of MPXV-infected hCO cultures revealed viral antigen signal accumulating at
158 regular intervals within elliptical swellings along infected filaments (Fig. 3a). Notably, these
159 structures were observed in 100% of independent batches of hCOs processed. Analogous
160 shape modulations, termed neuritic (i.e., axonal or dendritic) beading, have been postulated
161 to indicate degenerative processes and reported to accompany a variety of neuropathologies
162 including Alzheimer's disease, ischemia, and traumatic injuries[38-42]. Beaded filaments were
163 documented spanning for remarkable distances throughout the hCO tissue, both within and

164 outside of infection foci and swellings were observed to be present in both symmetric, lemon-
165 shaped and clam-shaped, asymmetric morphology, indicative of early and advanced stages of
166 beading[43]. Detailed analysis showed frequent co-localization of viral antigen accumulations
167 with neuronal marker TUJ1, both within swellings and affected filaments, suggesting gathering
168 of viral proteins along dendrites and axons (Fig. 3b). Aiming to confirm the injurious nature of
169 the observed structures, we analyzed the distribution of cleaved caspase-3, a pro-apoptotic
170 protein[44,45], within hCO tissue. In line with previous reports, we observed occasional cleaved
171 caspase-3 accumulation in neuritic varicosities as well as within associated cells (Fig. 3c),
172 supporting apoptotic processes accompanying the beading phenomenon.
173
174 **DISCUSSION**
175 In this study, we explored the neurobiology of MPXV in the human host using hCOs as an
176 advanced model of the human brain. Our data provides evidence that several neural cell
177 lineages are susceptible to MPXV infection, and the resulting replication leads to virus
178 propagation throughout the cerebral tissue. Moreover, evaluation of infectious virus titers in
179 intra- and extra-cellular compartments indicates a spread of MPXV via cell-to-cell contact in
180 hCOs. The identification of neuronal injury hallmarks and neurodegenerative signs
181 demonstrate the neurovirulence potential of MPXV in humans.
182 Despite MPXV infection cases being reported since 1970, studies investigating
183 pathomechanisms driving mpox disease are sparse. Moreso, current understanding of
184 processes leading to rare, but often severe complications in mpox affected individuals, shows
185 prominent gaps. We used hCOs of 70 to 95 days of age to model MPXV infection in the human
186 host, as we confirmed that prologued culture allows establishment of relevant cell diversity,
187 encompassing NPCs, neurons and astrocytes, within a highly complex environment. We show
188 that hCOs are highly susceptible to and allow active replication of MPXV, as demonstrated by
189 increasing cell-associated and released infectious virus, transmission electron microscopy,
190 and immunofluorescence. In line with recent reports[46], transmission electron microscopy
191 revealed presence of intracellular viral particles at several documented stages of replication,

192 including crescent membranes, immature viral particles, intracellular mature viral particles, and
193 extracellular viral particles. These findings show the establishment of MPXV replication
194 machinery in human cerebral tissue is possible and frequently occurs within infected hCO cells.
195 As previously described in Vero cells[33], we observed abundance of intracellular mature virions
196 over all other viral morphotypes, and documented their presence at different subcellular
197 locations, including in close proximity to viral factories, possibly indicating recently formed
198 virions, and adjacent to cell membranes. Furthermore, we confirmed the recurrent presence
199 of bundled cytoskeletal elements, which we frequently observed located in proximity to viral
200 factories. Cytoskeletal rearrangements have been recently reported in MPXV-infected Vero
201 cells[33], and cytoskeleton involvement in processes mediating viral distribution within infected
202 cells has been suggested[32,34,47,48], as well as during cell-to-cell transmission processes, as
203 actin tail formation[34,35,48]. We thus hypothesize that cytoskeletal condensations observed within
204 hCO cells might be involved in MPXV transport within the cell's cytoplasm.
205 In line with the establishment of a functional viral replication machinery within hCO cells,
206 immunofluorescence analysis showed a steady viral load increase in the course of infection,
207 reaching a peak around day 10 p.i. Viral antigen was initially visualized on the organoid's
208 surface, reaching deep into the tissue at advanced stages of infection. In addition, viral
209 particles were often detected localizing to distinct cell foci or streams, suggesting possible cell-
210 to-cell transmission, a prominent route exploited by orthopoxviruses, as vaccinia virus[34-36].
211 While no actin tails were visualized by transmission electron microscopy, intracellular mature
212 viral particles were observed within neurite sections in the processed tissue. In addition,
213 immunofluorescence analysis showed viral antigen localizing not only to cell somata, but also
214 to filaments of variable length, connecting distinct cells and dispersed within the organoid
215 tissue. Characterization of the strands showed that both TUJ1 positive neurites and F-actin
216 positive, but TUJ1 negative TNTs are found harboring viral particles within hCOs, suggesting
217 cell-to-cell transmission might occur through different routes in human neural tissue.
218 Comparison of cell-associated and released infectious virus further strengthened this
219 assumption. Indeed, intracellular viral loads were found to significantly exceed the amount of

220 released virus till day 10 p.i., with cell-associated viral particles steadily representing over 90%
221 of total infectious virus present in tissue and culture supernatant. Together, our findings
222 suggest that, as previously documented for the closely related vaccinia virus, MPXV
223 preferentially spreads directly from cell-to-cell and can exploit different mechanisms to spread
224 within human neural tissue. Furthermore, while our observations confirm the possible
225 transmission of MPXV through TNTs, as earlier documented for vaccinia virus[36], we
226 predominantly detected localization of viral antigen within TUJ1 positive neurites. This
227 observation suggests a previously undocumented mode of viral transmission for MPXV in the
228 human brain, in which viral particles can be transported from one cell to another through axons
229 and dendrites. Documented cytoskeletal alterations in proximity to viral factories could hint at
230 the mechanism of transportation of the virus, which could exploit the cell's fast axonal transport
231 machinery to move through the cytosol and reach distant locations, a mechanism observed to
232 be exploited by viruses of several families, most prominently *Herpesviridae*, *Flaviviridae*,
233 *Rhabdoviridae* and *Picornaviridae*[49], allowing viral dissemination while evading the host's
234 immune system.
235 In addition, our findings suggest possible injurious consequences of viral spread within cell
236 extensions. Viral antigen-containing filaments were often observed showing a series of
237 sequential swellings, termed neuritic beads. Analogous varicosities have been documented to
238 accompany diverse pathological states, including neurodegenerative disorders such as
239 Alzheimer's disease[38,39], ischemia[40] , traumatic injuries[41,42] and neurotropic virus infections[50-
240 52]. Beads are thought to originate from changes in membrane tension, and organelles,
241 cytoskeletal components as well as pathology-associated proteins have been observed to
242 sporadically pause or accumulate within them[43,53]. In line with these observations, we
243 confirmed occasional accumulation of cleaved caspase-3 within the somata and axonal
244 swellings of infected cells. Furthermore, varicosities have been observed to appear on axons
245 of trigeminal neurons upon pseudorabies virus cell attachment[54]. These swellings have been
246 suggested to represent sites of virus egress[54], promoting cell-to-cell spread[55], and could
247 possibly be accompanied by a deleterious interference with regular axonal functions[56]. It

248 seems reasonable to hypothesize that MPXV hijacks the cell's transport machinery, causing
249 cytoskeletal rearrangement, and exploits it to move through axons, leading to the generation
250 of neuritic beads that might represent sites of viral egress, finally causing neuronal injury by
251 hampering cell functions. Our findings furthermore indicate that cell death, and more precisely
252 apoptosis of infected neurons, can be triggered merely by viral presence in the absence of
253 immune cells. Future studies, focusing on elucidating the transport and egress dynamics of
254 MPXV within axons as well as the timing and process of bead formation, possibly through high-
255 resolution live-cell imaging of fluorescently tagged virions, will be required to fully comprehend
256 the underlying mechanisms and consequences of our findings.
257 Recently, Chailangkarn and colleagues, found induced pluripotent stem cell-derived neural
258 progenitor cells and astrocytes to be susceptible to MPXV infection in a two-dimensional
259 culture environment. This was demonstrated by changes in cell morphology and viability, as
260 well as increased viral loads detected in supernatant by qPCR over time[29]. In contrast, 14 and
261 45-day old neurons did not show productive MPXV infection[27]. In an unrefereed preprint,
262 human pluripotent stem cell-derived cortical neurons were however shown to be permissive to
263 MPXV infection by Bauer and colleagues, even if at a lower degree compared to astrocytes
264 and microglia[57]. In line with both reports, we confirmed susceptibility of both NPCs and
265 astrocytes to MPXV infection and found TUJ1-expressing neurons to be permissive to MPXV
266 infection as well. We propose that the prevalence of cell-associated neuronal spread of MPXV
267 through axonal transport provides a rationale for the previously reported low or undetected
268 viral replication within human neurons, suggested to resist viral infection to a certain degree,
269 based on the lack of strong increased detectable virus in culture supernatant. Further
270 investigation of the exact mechanisms driving the observed phenomenon could prove of
271 utmost importance in the development and identification of novel treatment options for patients
272 affected by MPXV encephalitis.
273 Taken together, we show that human neural tissue, modelled in a complex 3D environment, is
274 highly susceptible to infection with a contemporary clade IIb lineage MPXV isolate. We show
275 that viral replication factories are successfully established, resulting in a productive replication

276 of MPXV within organoid cells. Furthermore, we find that viral antigen localizes not only to cell
277 somata, but also to filaments of variable nature. We propose that MPXV preferentially spreads
278 from cell-to-cell, exploiting not only previously described mechanisms, but also through axonal
279 transport. Our hypothesis is further corroborated by the observation of serial swellings along
280 filaments, previously documented to represent sites of virus egress and cell-to-cell
281 transmission, as well as a sign of neuronal injury. Our findings identify a mechanism of MPXV
282 spread in the human cerebral tissue and constitute the basis for further exploration of the
283 neurobiology of orthopoxviruses.
284

285 **MATERIAL AND METHODS**

286 **Ethics statement**

287 In accordance with Articles 13 and 14 of the Federal Act on Research on Embryonic Stem
288 Cells, and Article 20 of the Ordinance on Research on Embryonic Stem Cells, the work with
289 human H1 ESC line was approved by the Cantonal Ethics Committee of Bern, Switzerland
290 under the authorization number R-FP-S-2-0023-0000.
291

292 **Maintenance of human embryonic stem cells**

293 The human H1 ESC line (WiCell) was cultured in feeder-free conditions and used to generate
294 hCOs employed in this study. ESCs were seeded onto untreated culture flasks (Sigma-Aldrich)
295 coated with Vitronectin XF (Stem Cell Technologies) and maintained in mTeSR Plus medium
296 (Stem Cell Technologies). Cells were maintained according to the manufacturer's
297 recommendations. Cells were passaged every 6-7 days applying 0.5 mM EDTA
298 (Thermofisher) in sterile Dulbecco's Phosphate Buffered Saline (DPBS, Gibco) for 4 minutes
299 at 37°C, 5% CO_2, followed by mechanical dissociation to obtain aggregates encompassing
300 approximately 5-8 cells. Regions with differentiated cells were scratched prior to cell
301 detachment. Cells were regularly checked and found negative for mycoplasma contamination.
302

303 **Generation of human cerebral organoids**

304 hCOs were generated using an adapted version of the previously published protocol by
305 Lancaster and colleagues[58]. Briefly, on day 0, ESCs were detached applying Accutase (Sigma-
306 Aldrich) for 4 minutes at 37 °C, 5% CO_2. Cells were dissociated by repeated pipetting till a
307 single-cell suspension was obtained. Cells were counted, centrifuged at 200 g for 5 minutes at
308 room temperature, and resuspended in the required volume of Formation Medium prepared
309 using the STEMdiff Cerebral Organoid Kit (Stem Cell Technologies) supplemented with 50 µM
310 Rho-associated protein kinase (ROCK) inhibitor Y-27632 (Stem Cell Technologies). The cell
311 suspension was distributed into ultra-low attachment 96-well plates (Corning), each well
312 containing 9'000 to 10'000 cells suspended in 100 uL of Formation Medium. The cultures were
313 left undisturbed for at least 24 hours. On day 2 and 4, 100 µL/well of Formation Medium without
314 ROCK inhibitor were added. On day 5, the formation of embryoid bodies (EBs) was confirmed
315 and EBs were transferred with wide-bore 200 uL tips to ultra-low attachment 24-well plates
316 (Corning), previously filled with 500 µL/well of Induction Medium, prepared using the STEMdiff
317 Cerebral Organoid Kit. On day 7, EBs were embedded into 30 µL droplets of Matrigel (Corning)
318 each and transferred into ultra-low attachment 6-well plates (Corning) containing 3 mL of
319 home-made Expansion Medium consisting of a 1:1 mixture of DMEM/F-12 (Gibco) and
320 Neurobasal Medium (Gibco) supplemented with 1:200 N2 (Gibco), 1:100 B27 minus vitamin A
321 (Gibco), 2.5 µg/mL insulin (Sigma-Aldrich), 1:100 GlutaMAX (Gibco), 1:200 MEM-NEAA
322 (Seraglob), 3.5 µL/L 2-mercaptoethanol (Sigma-Aldrich), and 1:100 Penicillin-Streptomycin
323 (Sigma-Aldrich, Gibco). On day 10, Expansion Medium was gently removed and replaced with
324 3.5 mL homemade differentiation medium consisting of a 1:1 mixture of DMEM/F-12 and
325 Neurobasal medium supplemented with 1:200 N2, 1:100 B27, 2.5 µg/mL insulin, 1:100
326 GlutaMAX, 1:200 MEM-NEAA, 3.5 uL/L 2-mercaptoethanol, 1:100 Penicillin-Streptomycin, and
327 0.5 ug/mL Amphotericin B (Gibco). From day 10 on, hCOs were cultured on an orbital shaker
328 at 65 rpm, in a 37 °C, 5% CO_2 incubator. Medium was changed every 2 to 3 days. hCOs
329 between 70-95 days old that passed the quality control criteria[58] were used for the experiments.
330 Criteria included hESC stemness of at least 80% of double positive cells for both stemness
331 markers SSEA-1 (Stem Cell Technologies) and TRA-1-60 (Stem Cell Technologies), which

332 was measured at day 0 by flow cytometry (FCM) assay. FCM acquisitions were performed on
333 a FACS Canto II (BD Bioscience) using the DIVA software and further analyzed with FlowJo
334 (TreeStar). Further quality control criteria included typical sizes corresponding to each
335 developing stage, brightening of outer layer at the EBs stage before embedding, and formation
336 of neural tube-like structures in Matrigel. All used media were warmed to room temperature
337 (20-25°C) before usage.
338
339 **Mpox virus propagation**
340 A primary isolate of MPXV belonging to clade IIb lineage isolated in 2022 was used for this
341 study (kindly provided by Prof. Dr. Isabela Eckerle, Geneva Center for Emerging Viral Diseases
342 and Division of Infectious Diseases, University Hospital of Geneva). The MPXV isolate was
343 passaged three times on Vero E6 cells to produce virus stocks. Briefly, 24 hours prior to
344 infection, Vero E6 cells were seeded in 75 cm^2 tissue culture flasks (TPP), at a density of $8x10^6$
345 cells per flask, and cultured at 37°C, 5% CO_2 in DMEM supplemented with GlutaMAX (Gibco),
346 10% fetal bovine serum (FBS, Gibco), 1 mM Sodium Pyruvate (Gibco) and 10 mM HEPES
347 (Gibco). On the day of infection, the culture medium was replaced with 5 mL of DMEM
348 supplemented with GlutaMAX and 2% FBS, and the required amount of virus stock was added.
349 Cells were placed on an orbital shaker moving at 60 rpm for 1 hour at 37°C, 5% CO_2. Following
350 incubation, 15 mL DMEM supplemented with GlutaMAX and 2% fetal bovine serum were
351 added. Cells were incubated at 37°C, 5% CO_2 and inspected daily for signs of cytopathic effect
352 (CPE). At day 3 p.i. (i.e., when a CPE of around 80% of cells was observed) flasks were frozen
353 at -70°C, to release cell-associated viral particles. Viral suspensions were subsequently
354 thawed, collected in 50 mL conical tubes, and centrifuged at 1000 g for 10 minutes at 4°C to
355 remove cell debris. Supernatants were aliquoted and stored at -70°C till further use. Mock
356 control stocks were generated in parallel, following the same procedures, with omission of
357 virus inoculum. All procedures involving MPXV handling were carried out in biosafety level 3
358 (BSL3) conditions at the Institute of Virology and Immunology (University of Bern, Switzerland)
359 by trained personnel provided with appropriate personal protective equipment.

360

361 **Mpox virus titration**

362 Viral stocks, organoid supernatants and homogenized organoids were titrated on Vero E6 cells
363 in a 96-well plate format. 24 hours prior to titration, the required number of 96 well plates (TPP)
364 were seeded with a suspension of Vero E6 cells at a density of $2x10^4$ cells per well. Serial
365 dilutions were performed in DMEM supplemented with GlutaMAX, 10% FBS,1 mM Sodium
366 Pyruvate, 10 mM HEPES (Gibco), and 1% Penicillin-Streptomycin, starting at a dilution of 1:10.
367 Cell supernatant was aspirated, and the dilutions transferred on the previously seeded cells.
368 Cells were incubated for 72 hours at 37°C, 5% CO_2. For readout, the inoculum was aspirated,
369 cells washed once with 200 μL PBS (Sigma-Aldrich), fixed for 15 minutes by immersion in 4%
370 paraformaldehyde (PFA, Sigma-Aldrich), and subsequently stained for 10 minutes with crystal
371 violet. Plates were washed with tap water and left to dry prior to readout. Viral titers were
372 calculated as $TCID_{50}$ per mL using the Reed and Muench method. For titration of released viral
373 loads, culture supernatant was collected at selected time points and stored at -70°C until
374 further analysis. Analogously, for quantification of cell-associated infectious virus, one
375 organoid per time
376 point was randomly sampled, washed with sterile DPBS and transferred into a 1.5 mL screw
377 cap tube containing 1 mL of sterile DPBS. The sample was frozen at -70°C. For analysis, the
378 thawed hCO was dissociated thoroughly by pipetting up and down, until no cell clumps were
379 visible any longer. The sample was centrifuged at 450 g for 5 minutes at 4°C and the
380 supernatant used for titration. For normalization, obtained released viral titers were multiplied
381 by the volume of medium per well and divided by the number of hCOs per well, to obtain
382 released infectious virus per hCO. Analogously, cell-associated viral titers were multiplied by
383 the total sample volume and divided by the number of organoids per sample, to obtain cell-
384 associated infectious virus per hCO.

385

386 **Human cerebral organoids infection**

387 hCOs were infected at 70 to 95 days of age in a 6-well plate format with an MOI of 0.1
388 $TCID_{50}$/cell. Briefly, virus suspension was prepared by adding the required amount of virus
389 stock to organoid Maturation Medium (see “Generation of human cerebral organoids”) in a 50
390 mL conical tube to obtain a homogeneous suspension of 3 mL per well. Mock treatment was
391 prepared analogously. Organoid culture medium was removed from all wells and replaced with
392 the inoculum. hCOs were incubated for 2 hours at 37°C, 5% CO_2, constantly shaking at 65
393 rpm. hCOs were subsequently washed three times with 3 mL of sterile DPBS. 4 mL of fresh
394 organoid Maturation Medium were added to each well, and hCOs were placed back in the
395 incubator at 37°C, 5% CO_2, shaking at 65 rpm. Supernatant samples were taken 2 hours post
396 washing to confirm baseline infectious viral loads. Further tissue and culture supernatant
397 samples were collected at selected time points and stored at -70°C until further analysis. All
398 media and reagents were allowed to reach room temperature prior to application of hCOs.
399
400 **Human cerebral organoids cryopreservation and immunofluorescence**
401 hCOs were processed using an adapted version of the protocol “Cryogenic Tissue Processing
402 and Section Immunofluorescence of Cerebral Organoids” provided by STEMCELL
403 Technologies. For immunofluorescence, hCOs were washed twice with PBS and fixed in 4%
404 PFA. Next, hCOs were washed three times with PBS. For cryogenic preservation, hCOs were
405 subsequently incubated at 4°C in a 30% sucrose (Sigma-Aldrich) in PBS solution until
406 organoids were observed to sink to the bottom of the tube. Equilibrated hCOs were embedded
407 and incubated in a 7.5% gelatin, 10% sucrose in PBS solution for 1 hour at 37°C, to avoid
408 polymerization. In the meantime, a mixture of dry ice and 100% ethanol was prepared. hCOs
409 and gelatin were subsequently transferred to a Crymold (Biosystems Switzerland AG) and,
410 after initial polymerization at room temperature, carefully placed on the surface of the (no
411 longer boiling) mixture of dry ice and ethanol. Once completely frozen, embedded hCOs were
412 transferred to -80°C for long term storage. For immunofluorescence, cryopreserved hCOs
413 were processed into 18 µm thin slices using a Leica CM1950 cryostat and placed on
414 SuperFrost Plus Adhesion slides (Epredia). Slides were stored at -20°C till staining. For

415 staining, sections were allowed to reach room temperature prior to processing. To dissolve
416 gelatin, slides were subsequently incubated for 10 minutes in a 37°C pre-warmed mixture of
417 0.1% Tween-20 (Sigma-Aldrich) in PBS. hCO sections were encircled using a ReadyProbes
418 Hyrophobic Barrier Pap Pen (Thermo Fisher Scientific) and blocked with a 5% donkey serum
419 (Abcam) in 0.1% Tween-20 in PBS solution for 1 hour at room temperature. Primary antibodies
420 were resuspended in 0.1% Tween-20 in PBS supplemented with 5% BSA at the following
421 dilutions: TUJ1 (BioLegend, 801202, 1:400), SOX2 (Invitrogen, 14-9811-82, 1:200), GFAP
422 (Invitrogen, PA1-10004, 1:200), vaccina virus i.e. MPXV A27L protein (OriGene Technologies,
423 Inc BP1076, 1:1000), cleaved caspase-3 (arigo Biolaboratories Crop., ARG66888, 1:200).
424 Blocking buffer was removed, 100 uL of primary antibody solution were added to each section
425 and slides were allowed to incubate at 4°C overnight. On the following day, primary antibody
426 solution was removed by gently tapping slides on paper towels and sections were washed
427 three times for 5 minutes by immersion in 0.1% Tween-20 in PBS. Secondary antibodies were
428 resuspended in 0.1% Tween-20 in PBS at the following dilutions: anti-mouse AF488
429 (Invitrogen, A21131, 1:200), anti-mouse AF647 (Invitrogen, A2124, 1:200), anti-rat AF647
430 (Invitrogen, A21247, 1:500), anti-chicken AF546 (Invitrogen, A11040, 1:200), anti-rabbit
431 AF488 (Jackson ImmunoResearch Europe Ltd., 711-545-152, 1:200), anti-rabbit AF546
432 (Invitrogen, A11035, 1:200), anti-rabbit AF647 (Invitrogen, A21245, 1:200). For nuclear and F-
433 actin staining, DAPI (Sigma-Aldrich) and Rhodamine Phalloidin (Invitrogen, R415, 1:200) were
434 added to the mixture. Sections were incubated with secondary antibodies for 2 hours at room
435 temperature. Slides were subsequently washed three more times for 5 minutes by immersion
436 in 0.1% Tween-20 in PBS and mounted in EMS Shield Mount with DABCO (Electron
437 Microscopy Sciences). Imaging was performed using a Carl Zeiss LSM710 confocal
438 microscope at the microscopy imaging center (MIC) of the University of Bern, Switzerland.
439 Images were analyzed using ImageJ.
440
441 **Transmission electron microscopy**

442 For transmission electron microscopy, hCOs were fixed using a 2.5% glutaraldehyde and 2%
443 PFA solution in organoid Maturation Medium for a duration of 1 day at 4°C. Subsequently, the
444 fixation solution was replaced with 4% PFA, and samples stored at 4°C until further processing.
445 hCOs were cut into 1 mm3 cubes and immerged in a 1% osmium tetroxide (Electron
446 Microscopy Sciences) solution in ddH_2O for 1 hour at room temperature. After washing three
447 times with ddH_2O, samples were progressively dehydrated in a graded ethanol series, starting
448 from 50% and progressing to 70%, 80%, 90%, and finally 100% ethanol. The samples were
449 then embedded in epoxy resin (EM0300, Sigma-Aldrich) and left to polymerize for 8 hours at
450 70℃. Ultrathin sections of resin-embedded tissue were prepared using a Leica EM UC7
451 ultramicrotome. Sections of 70 nm were collected on EM grids (G100H-Cu, Electron
452 Microscopy Sciences) and processed using a 2% uranyl acetate and 0.5% lead citrate solution
453 for contrast enhancement. The obtained sections were imaged using a CM-100 transmission
454 electron microscope (Philips) at 80 kV. Images were analyzed using ImageJ.
455
456 **Statistical analysis**
457 GraphPad Prism 9 software was used for statistical analysis and graph generation. Non-
458 parametrical Mann-Whitney U test was used to assess significance of detected values. $p<0.05$
459 was considered statistically significant.
460
461 **ACKNOWLEDGEMENTS**
462 We would like to extend our gratitude to the Geneva Center for Emerging Viral Diseases, the
463 Division of Infectious Diseases and Prof. Dr. Isabela Eckerle for providing the clade IIb MPXV
464 isolate used in this study. This work was supported by a grant from the Multidisciplinary Center
465 for Infectious Diseases of the University of Bern (to M.P.A.) and by intramural funding of the
466 Institute of Virology and Immunology.
467
468 **DECLARATION OF INTEREST**
469 The authors declare no competing interests.

DATA AVAILABILITY STATEMENT

The data generated and analyzed during the current study are available from the corresponding author on reasonable request.

AUTHOR CONTRIBUTIONS

I.S.P., A.F., D.B., and M.P.A. conceptualized and designed the project. I.S.P., A.F., Y.C.C., B.O.I.E., T.D., and B.Z. conducted the investigations. I.S.P., A.F., Y.C.C., B.O.I.E., T.D., B.Z., A.G., S.S., C.W., R.Z. D.J., F.B., and O.B.E. developed the methodology and provided reagents. M.P.A., I.S.P., A.F., Y.C.C., B.O.I.E., and T.D. curated and analyzed the data. I.S.P., A.F., and M.P.A. wrote the original manuscript. All authors reviewed, edited, and approved the manuscript.

REFERENCES

1. Organization, W.H. 2022 Mpox (Monkeypox) Outbreak: Global Trends. (2022).
2. Thornhill, J.P.*, et al.* Monkeypox Virus Infection in Humans across 16 Countries - April-June 2022. *The New England Journal of Medicine* **387**, 679-691 (2022).
3. Perez Duque, M.*, et al.* Ongoing monkeypox virus outbreak, Portugal, 29 April to 23 May 2022. *Eurosurveillance* **27**(2022).
4. Girometti, N.*, et al.* Demographic and clinical characteristics of confirmed human monkeypox virus cases in individuals attending a sexual health centre in London, UK: an observational analysis. *The Lancet Infectious Diseases* **22**, 1321-1328 (2022).
5. Badenoch, J.B.*, et al.* Neurological and psychiatric presentations associated with human monkeypox virus infection: A systematic review and meta-analysis. *EClinicalMedicine* **52**, 101644 (2022).
6. Jezek, Z., Szczeniowski, M. & Paluku, K.M. Human Monkeypox: Clinical Features of 282 Patients. *The Journal of Infectious Diseases* **156**, 2 (1987).
7. Kozlov, M. How deadly is monkeypox? What scientists know. *Nature* **609**, 663 (2022).
8. Pastula, D.M.*, et al.* Two Cases of Monkeypox-Associated Encephalomyelitis - Colorado and the District of Columbia, July-August 2022. *Morbidity and Mortality Weekly Report* **71**, 1212 - 1215 (2022).

9. Viguier, C.*, et al.* A severe monkeypox infection in a patient with an advanced HIV infection treated with tecovirimat: clinical and virological outcome. *International Journal of Infectious Diseases* **125**, 135-137 (2022).

10. Cole, J.*, et al.* Monkeypox encephalitis with transverse myelitis in a female patient. *Lancet Infect Dis* (2022).

11. Rodriguez, A., Rodriguez, L.C. & Bastidas, N. Acute disseminated encephalomyelitis in a patient with monkeypox: a case report and radiological findings. *Emerging Radiology* (2022).

12. Marin-Medina, D.S.*, et al.* Encephalomyelitis in a patient with monkeypox: an unusual complication. *Journal of Neurovirology* **29**, 237-240 (2023).

13. Sharma, R., Nguyen-Luu, T., Dhaubhadel, P., Sharma, A. & Naik, R. A Rare Co-occurrence of Monkeypox Encephalitis and Neurosyphilis. *Cureus* **15**, e35945 (2023).

14. Yadav, P.D.*, et al.* An imported case of fatal encephalitis associated with mpox virus infection, India, July 2022. *Journal of Medical Virology* **95**, e28755 (2023).

15. Huston, C.L.*, et al.* Monkeypox zoonotic associations: insights from laboratory evaluation of animals associated with the multi-state us outbreak. *The American Journal of Tropical Medicine and Hygiene* **76**(2007).

16. Kulesh, D.A.*, et al.* Monkeypox virus detection in rodents using real-time 3'-minor groove binder TaqMan assays on the Roche LightCycler. *Laboratory Investigation* **84**, 1200-1208 (2004).

17. Falendysz, E.A.*, et al.* Evaluation of monkeypox virus infection of black-tailed prairie dogs (Cynomys ludovicianus) using in vivo bioluminescent imaging. *Journal of Wildlife Diseases* **50**, 524-536 (2014).

18. Hutson, C.L.*, et al.* Monkeypox disease transmission in an experimental setting: prairie dog animal model. *PLoS One* **6**, e28295 (2011).

19. Sejvar, J.J.*, et al.* Human Monkeypox Infection: A Family Cluster in the Midwestern United States. *The Journal of Infectious Diseases* **190**, 1833-1840 (2004).

20. Lancaster, M.A.*, et al.* Cerebral organoids model human brain development and microcephaly. *Nature* **501**, 373-379 (2013).

21. Sullivan, K.F. & Cleveland, D.W. Identification of conserved isotype-defining variable region sequences for four vertebrate beta tubulin polypeptide classes. *The Proceedings of the National Academy of Sciences* **83**, 4327-4331 (1986).

22. Sullivan, K.F. Structure and Utilization of Tubulin Isotypes. *Annual review of cell biology* **4**, 687-716 (1988).

23. Burgoyne, R.D., Cambray-Deakin, M.A., Lewis, S.A., Sarkar, S. & Cowan, N.J. Differential distribution of beta-tubulin isotypes in cerebellum. *The EMBO Journal* **7**, 2311-2319 (1988).

24. Lee, M.K., Tuttle, J.B., Rebhun, L.I., Cleveland, D.W. & Frankfurter, A. The Expression and Posttranslational Modification of a Neuron-Specific beta-Tubulin Isotype During Chick Embryogenesis. *Cell Motility and the Cytoskeleton* **17**, 118-132 (1990).

541 25. Zappone, M.V., *et al.* Sox2 regulatory sequences direct expression of a β-geo
542 transgene to telencephalic neural stem cells and precursors of the mouse embryo,
543 revealing regionalization of gene expression in CNS stem cells. *Development* **127**,
544 2367-2382 (2000).

545 26. Graham, V., Khudyakov, J., Ellis, P. & Pevny, L. SOX2 functions to maintain neural
546 progenitor identity. *Neuron* **39**, 749-765 (2003).

547 27. Eng, L.F., Vanderhaeghen, J.J., Bignami, B. & Gerstl, B. An acidic protein isolated from
548 fibrous astrocytes. *Brain Research* **28**(1971).

549 28. Nascimento, J.M., *et al.* Human Cerebral Organoids and Fetal Brain Tissue Share
550 Proteomic Similarities. *Frontiers in Cell and Developmental Biology* **7**, 303 (2019).

551 29. Chailangkarn, T., *et al.* Monkeypox virus productively infects human induced
552 pluripotent stem cell-derived astrocytes and neural progenitor cells. *Journal of Infection*
553 **85**, 702-769 (2022).

554 30. Doms, R.W., Blumenthal, R. & Moss, B. Fusion of Intra- and Extracellular Forms of
555 Vaccinia Virus with the Cell Membrane. *Journal of Virology* **64**, 4884-4892 (1990).

556 31. Chung, C.-S., Hsiao, Y.-C., Chang, U.-S. & Chang, W. A27L Protein Mediates Vaccinia
557 Virus Interaction with Cell Surface Heparan Sulfate. *Journal of Virology* **72**, 1577–1585
558 (1998).

559 32. Sanderson, C.M., Hollinshead, M. & Smith, G.L. The vaccinia virus A27L protein is
560 needed for the microtubuledependent transport of intracellular mature virus particles.
561 *Journal of General Virology* **81**, 47-58 (2000).

562 33. Witt, A.S.A., *et al.* Ultrastructural analysis of monkeypox virus replication in Vero cells.
563 *Journal of Medical Virology* **95**, e28536 (2023).

564 34. Stokes, G.V. High-Voltage Electron Microscope Study of the Release of Vaccinia Virus
565 from Whole Cells. *Journal of Virology* **18**(1976).

566 35. Cudmore, S., Cossartt, P., Griffiths, G. & Way, M. Actin-based motility of vaccinia virus.
567 *Nature* **378**, 636–638 (1995).

568 36. Xiao, M., Xu, N., Wang, C., Pang, D.W. & Zhang, Z.L. Dynamic monitoring of
569 membrane nanotubes formation induced by vaccinia virus on a high throughput
570 microfluidic chip. *Scientific Reports* **7**, 44835 (2017).

571 37. Valappil, D.K., Raghavan, A. & Nath, S. Detection and Quantification of Tunneling
572 Nanotubes Using 3D Volume View Images. *Journal of Visualized Experiments* (2022).

573 38. Ohgami, T., Kitamoto, T. & Tateishi, J. Alzheimer's amyloid precursor protein
574 accumulates within axonal swellings in human brain lesions. *Neuroscience Letters* **136**,
575 75-78 (1992).

576 39. Wirths, O., Weis, J., Szczygielski, J., Multhaup, G. & Bayer, T.A. Axonopathy in an
577 APP/PS1 transgenic mouse model of Alzheimer's disease. *Acta Neuropathologica* **111**,
578 312-319 (2006).

579 40. Hori, N. & Carpenter, D.O. Functional and Morphological Changes Induced by
580 Transient in Vivo Ischemia. *Experimental Neurology* **129**, 279-289 (1994).

581 41. Pavlidis, M., Stupp, T., Naskar, R., Cengiz, C. & Thanos, S. Retinal Ganglion Cells
582 Resistant to Advanced Glaucoma: A Postmortem Study of Human Retinas with the
583 Carbocyanine Dye DiI. *Investigative Ophthalmology & Visual Science* **44**, 5196-5205
584 (2003).

585 42. Li, Y.*, et al.* A Precise, Controllable in vitro Model for Diffuse Axonal Injury Through
586 Uniaxial Stretch Injury. *Frontiers in Neuroscience* **13**, 1063 (2019).

587 43. Datar, A.*, et al.* The Roles of Microtubules and Membrane Tension in Axonal Beading,
588 Retraction, and Atrophy. *Biophysical Journal* **117**, 880-891 (2019).

589 44. Fernandes-Alnemri, T., Litwack, G. & Alnemri, E.S. CPP32, a novel human apoptotic
590 protein with homology to Caenorhabditis elegans cell death protein Ced-3 and
591 mammalian interleukin-1 beta-converting enzyme. *Journal of Biological Chemistry* **269**,
592 30761-30764 (1994).

593 45. Waterhouse, N.*, et al.* Heteronuclear ribonucleoproteins C1 and C2, components of the
594 spliceosome, are specific targets of interleukin 1beta-converting enzyme-like proteases
595 in apoptosis. *J Biol Chem* **271**, 29335-29341 (1996).

596 46. Ormel, P.R.*, et al.* Microglia innately develop within cerebral organoids. *Nature*
597 *Communications* **9**, 4167 (2018).

598 47. Hiller, G., Weber, K., Schneider, L., Parajsz, C. & Jungwirth, C. Interaction of
599 assembled progeny pox viruses with the cellular cytoskeleton. *Virology* **98**, 142-153
600 (1979).

601 48. Hollinshead, M.*, et al.* Vaccinia virus utilizes microtubules for movement to the cell
602 surface. *Journal of Cell Biology* **154**, 389-402 (2001).

603 49. Taylor, M.P. & Enquist, L.W. Axonal spread of neuroinvasive viral infections. *Trends in*
604 *Microbiology* **23**, 283-288 (2015).

605 50. Jacomy, H., Fragoso, G., Almazan, G., Mushynski, W.E. & Talbot, P.J. Human
606 coronavirus OC43 infection induces chronic encephalitis leading to disabilities in
607 BALB/C mice. *Virology* **349**, 335-346 (2006).

608 51. Hirano, M.*, et al.* Tick-borne flaviviruses alter membrane structure and replicate in
609 dendrites of primary mouse neuronal cultures. *Journal of General Virology* **95**, 849-861
610 (2014).

611 52. Jackson, A.C. Diabolical effects of rabies encephalitis. *Journal of Neurovirology* **22**, 8-
612 13 (2016).

613 53. Yong, Y., Hunter-Chang, S., Stepanova, E. & Deppmann, C. Axonal spheroids in
614 neurodegeneration. *Molecular and Cellular Neuroscience* **117**, 103679 (2021).

615 54. De Regge, N.*, et al.* Alpha-herpesvirus glycoprotein D interaction with sensory neurons
616 triggers formation of varicosities that serve as virus exit sites. *The Journal of Cell*
617 *Biology* **174**, 267-275 (2006).

618 55. Tomishima, M.J. & Enquist, L.W. In vivo egress of an alphaherpesvirus from axons.
619 *Journal of Virology* **76**, 8310-8317 (2002).

620 56. Hatch Berth, S., Leopold, P.L. & Morfini, G. Virus-induced neuronal dysfunction and
621 degeneration. *Frontiers in Bioscience-Landmark* **14**(2009).

622 57. Bauer, L., *et al.* Dissecting the neurotropism and neurovirulence of MPXV using human
623 stem cell-based models. *bioRxiv* (2023).

624 58. Lancaster, M.A. & Knoblich, J.A. Generation of cerebral organoids from human
625 pluripotent stem cells. *Nat Protoc* **9**, 2329-2340 (2014).
626

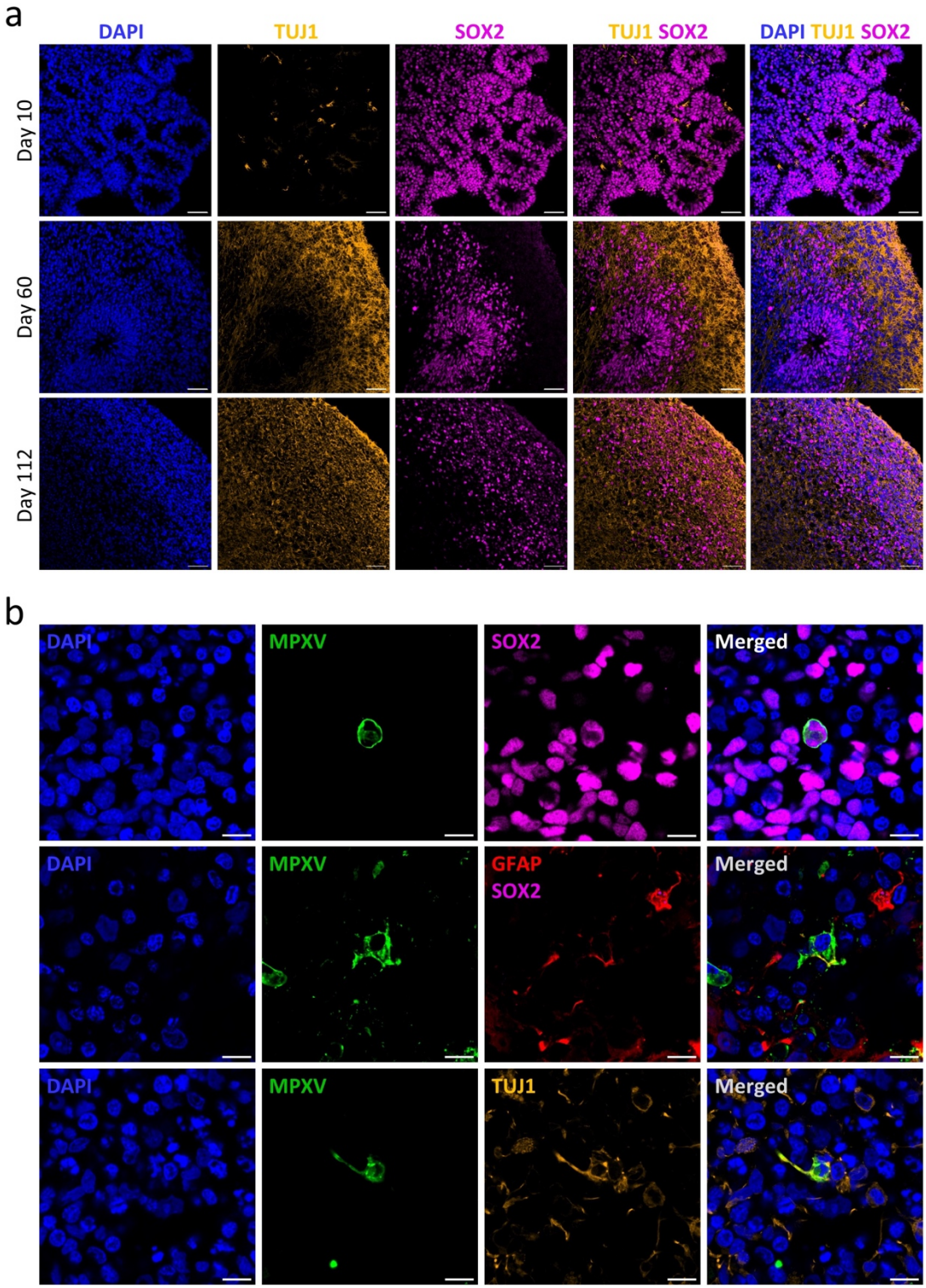

627

628 **Figure 1: MPXV has a broad cellular tropism in hCOs.** (a) Representative micrographs
629 showing the cell diversity and morphology of ESC-derived hCOs at selected developmental
630 time points (10, 60, and 112 days). Selected markers of neural progenitors (SOX2, pink) and
631 neurons (TUJ1, yellow) are presented. DAPI, blue. Scale bar, 50 µm. (b) Representative
632 micrographs illustrating the target cells of MPXV in 70-95 days old hCOs 10 days p.i. with a

633 clade IIb lineage isolate at a MOI of 0.1 $TCID_{50}$/cell. MPXV, green; SOX2, pink; GFAP, red;

634 DAPI, blue. Scale bar, 10 μm.

635

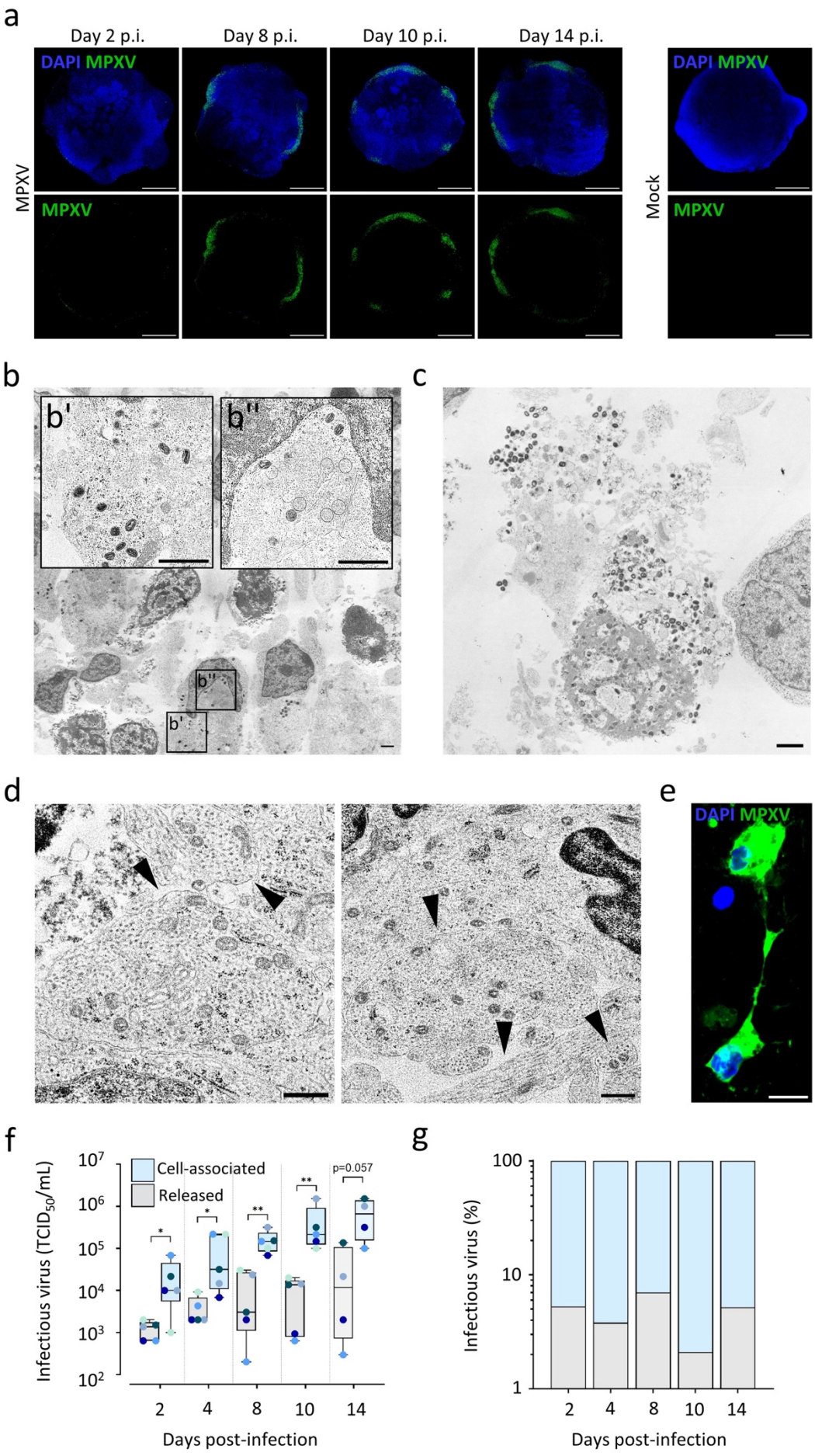
a
Day 2 p.i.
Day 8 p.i.
Day 10 p.i.
Day 14 p.i.
DAPI MPXV
MPXV
MPXV
DAPI MPXV
Mock
MPXV
b
b'
b''
b''
b'
c
d
e
DAPI MPXV
f
Infectious virus (TCID50/mL)
Cell-associated
Released
p=0.057
Days post-infection
g
Infectious virus (%)
Days post-infection

636

637 **Figure 2: Productive MPXV infection and cell-to-cell transmission in hCOs.** (a)
638 Representative micrographs of 70-95 days old hCOs infected with a clade IIb lineage MPXV
639 isolate at a rate of 0.1 $TCID_{50}$/cell. Infection was followed by immunofluorescence from 2 to 14
640 days p.i. by whole-organoid imaging. MPXV, green; DAPI, blue. Scale bar, 1000 µm. (b-d)
641 Representative images acquired by transmission electron microscopy at 10 days p.i. of 95
642 days old hCOs infected with a clade IIb lineage MPXV isolate with an MOI of 0.1 $TCID_{50}$/cell.
643 (b') Magnification demonstrating the presence of intracellular mature virions within cells. Scale
644 bar, 1 µm (b'') Magnification showing the presence of viral particles at different stages of
645 development alongside with perinuclear viral factories, displaying cytoskeletal condensations.
646 Scale bar, 1 µm. (c) Illustration of degenerative signs, bursting and release of intracellular
647 compartment containing high amounts of mpox virions. Scale bar, 1 µm. (d) MPXV particles
648 were observed localizing to neurites in infected hCO tissue. Black arrowheads indicate
649 exemplary virion-harboring neurites. Scale bar, 0.5 µm. (e) Representative image of the
650 detection by immunofluorescence of MPXV signal within neural filaments of interconnected,
651 distinct cells. MPXV, green; DAPI, blue. Scale bar, 10 µm. (f) Cell-associated and released
652 infectious MPXV 2 to 14 days p.i. of 70-95 days old hCOs infected with a clade IIb lineage
653 isolate at a rate of 0.1 $TCID_{50}$/cell. Boxplots indicate median value (centerline) and interquartile
654 ranges (box edges), with whiskers extending to the lowest and the highest values. Each symbol
655 represents an individual organoid (n=4-5 independent organoid batches). Mann-Whitney U test
656 was applied to compare groups. *$p<0.05$, **$p<0.01$. (g) Data presented in (f) represented as
657 percentage of total infectious virus content.
658

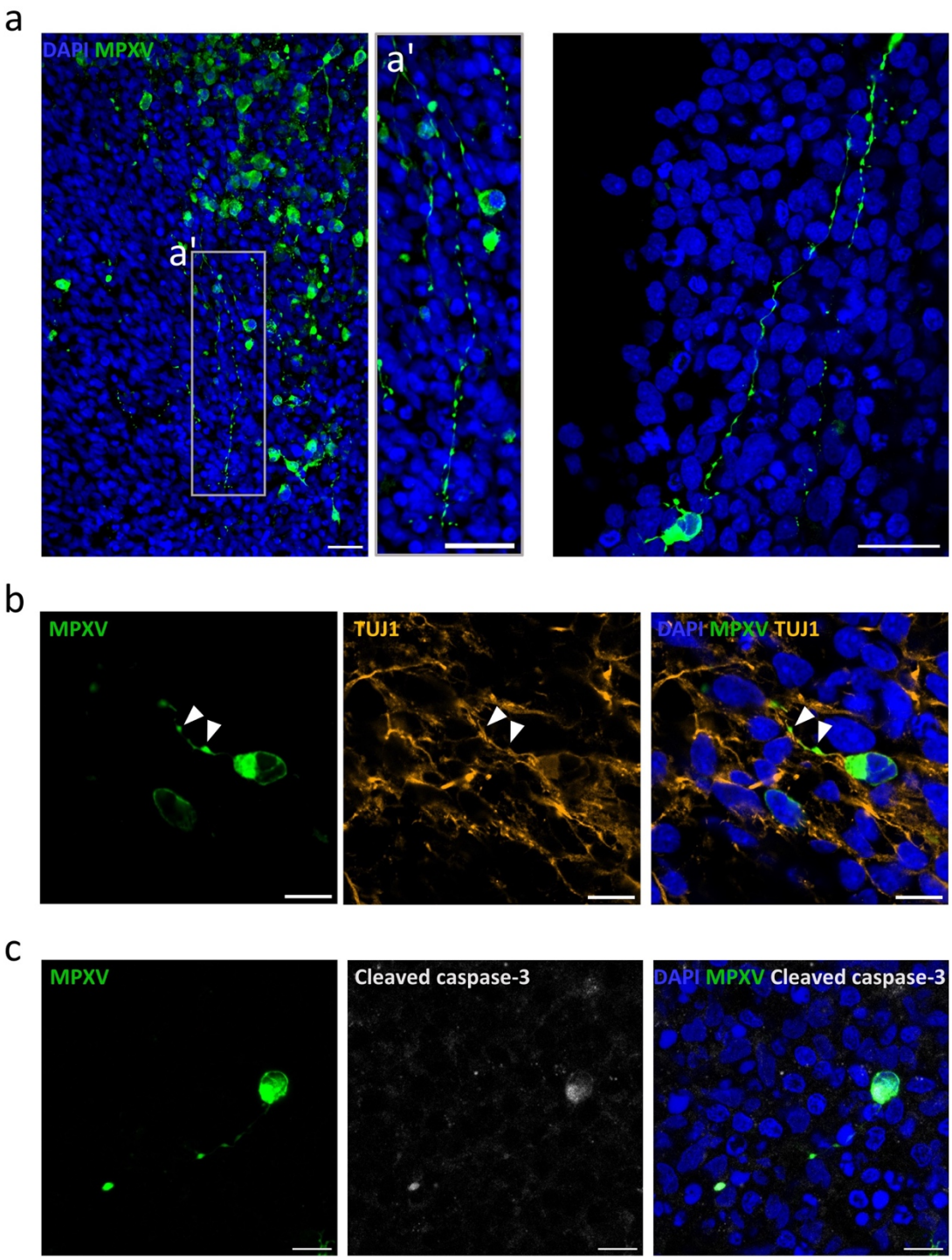

Figure 3: MPXV causes neuritic beading and injury in hCOs. (a-c) Immunofluorescene analysis 8-14 days p.i. of 70 days old hCOs exposed to a clade IIb lineage MPXV isolate at a rate of 0.1 $TCID_{50}$/cell. (a) Representative micrographs showing viral antigen accumulating within regularly interspaced swellings (beads) on filaments, spanning over long distances within the tissue. MPXV, green; DAPI, blue. Scale bar, 25 µm. (b) Representative micrographs of beaded filaments harboring mpox virions co-localizing with the neuronal marker TUJ1 in

666 both filaments and varicosities. MPXV, green; TUJ1, orange; DAPI, blue. Scale bar, 10 μm. (c)
667 Representative micrographs of neuritic beads and soma of an infected cell accumulating
668 cleaved caspase-3. MPXV, green; cleaved caspase-3, white; DAPI, blue. Scale bar, 10 μm.
669
670

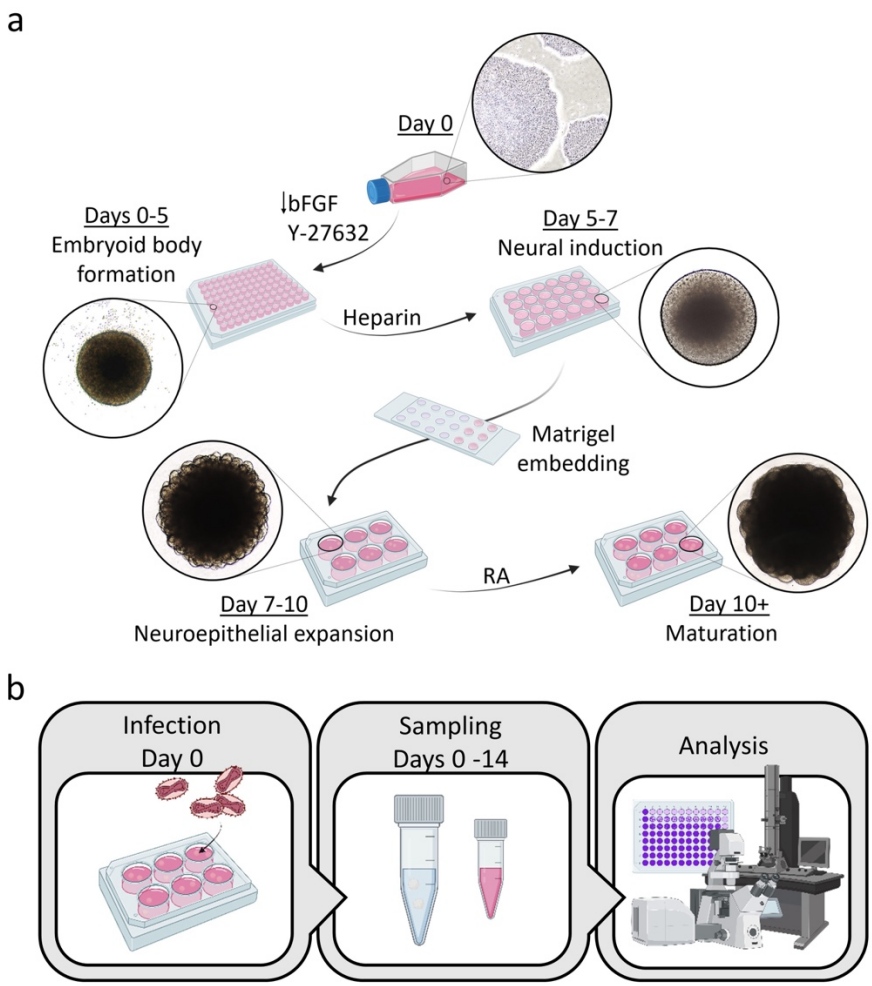

Supplementary Figure 1: Experimental design for hCOs generation and infection. (a) At day 0 ESCs were dissociated, resuspended in Formation Medium and distributed at a density of 9'000-10'000 cells per well in ultra-low attachment 96-well plates for EB formation. After 5 days, EBs were transferred to Induction Medium for neural induction. At day 7, EBs were embedded into Matrigel and transferred to ultra-low attachment 6-well plates in Expansion Medium. At day 10, hCOs were transferred to Maturation Medium and moved to an orbital shaker for further development. (b) 70 to 95 days old hCOs were infected with a clade IIb isolate at an MOI of 0.1 $TCID_{50}$/cell. Supernatant and tissue samples were taken at regular intervals for a period of up to 14 days, prior to analysis.

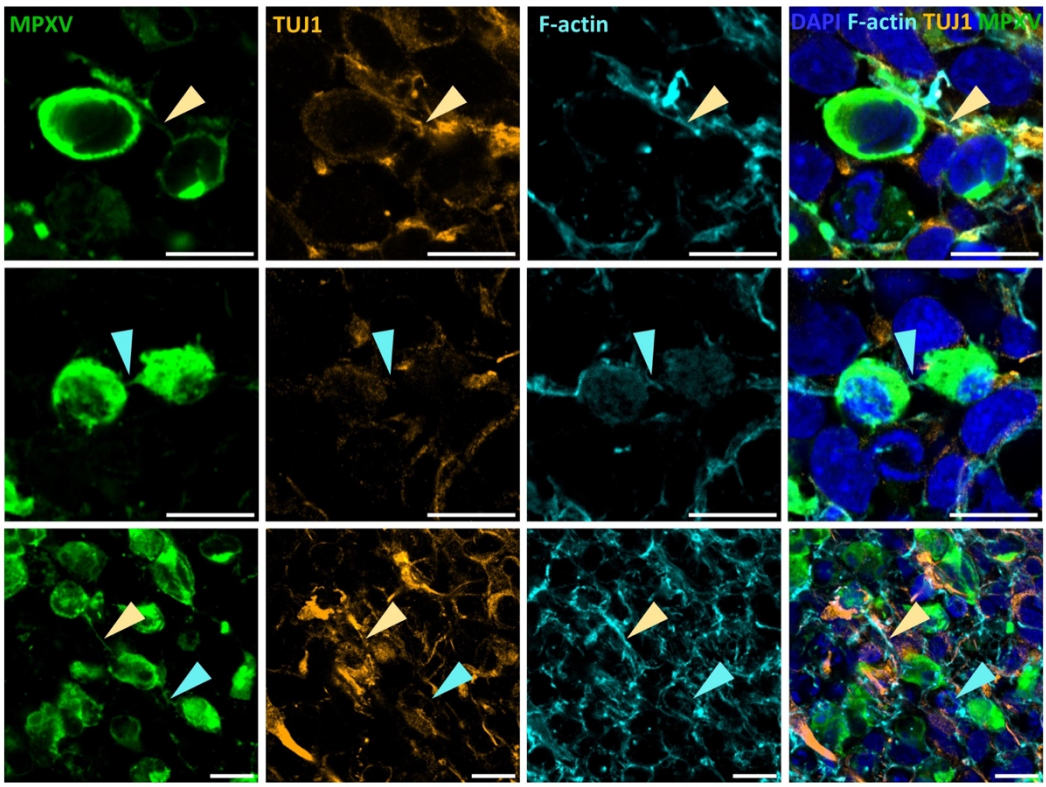

Supplementary Figure 2: Filaments interconnecting cells in hCOs comprise both TNTs and neurites. Representative micrographs showing the filaments connecting MPXV antigen positive cells and displaying diverse TUJ1 and F-actin patterns. Some filaments were observed showing expression of both markers (yellow arrowheads), indicative of their neuritic nature, others lacked TUJ1 signal, indicative of TNTs (blue arrowheads). MPXV, green; TUJ1, orange; F-actin, cyan blue; DAPI, dark blue. Scale bar, 10 µm.